This document is the accepted manuscript version of the following article:

Zhu, P., Brunner, S., Zhao, S., Griffa, M., Leemann, A., Toropovs, N., … Lura, P. (2019). Study of physical properties and microstructure of aerogel-cement mortars for improving the fire safety of high-performance concrete linings in tunnels. Cement and Concrete Composites, 104, 103414 (11 pp.). https://doi.org/10.1016/j.cemconcomp.2019.103414

This manuscript version is made available under the CC-BY-NC-ND 4.0 license http://creativecommons.org/licenses/by-nc-nd/4.0/

Study of physical properties and microstructure of aerogel-cement mortars for improving the fire safety of high-performance concrete linings in tunnels

Pinghua Zhu[1,2], Samuel Brunner[2], Shanyu Zhao[2], Michele Griffa[2], Andreas Leemann[2], Nikolajs Toropovs[2,3], Andreas Malekos[2,4], Matthias M. Koebel[2], Pietro Lura[2,5]*

[1] School of Environmental and Safety Engineering, Changzhou University, Changzhou, Jiangsu 213164, PR China.

[2] Empa, Swiss Federal Laboratories for Materials Science and Technology, CH-8600, Dübendorf, Switzerland. [3] Riga Technical University, Institute of Materials and Structures, Riga, Latvia.

[4] School of Physics and Astronomy, The University of Edinburgh, EH8 9YL, Edinburgh, UK

[5]ETH Zurich, Swiss Federal Institute of Technology Zurich, Zurich, Switzerland

***To whom correspondence should be addressed** pietro.lura@empa.ch

Abstract

In high-performance concrete (HPC) subjected to high temperature during tunnel fires, the build-up of vapor pressure due to dehydration of the cement hydration products cannot be re-lieved due to the very low porosity and permeability of this type of concrete, often resulting in explosive spalling. Explosive spalling may cause devastating damage of the tunnel structure, which threatens both, civilians and emergency response units.

This work suggests a potential application of silica aerogel in the protection of concrete linings, which consists in decorating the surface of HPC structures with a highly-insulating aerogel-cement mortar layer, with the aim of delaying the heating of the HPC and extending the performance of the main concrete structure of the tunnel under fire. The main aim of this study is investigating the impact of the microstructure, with special focus on the pore structure, on the thermal conductivity and the mechanical properties of the aerogel mortars. In particular, the integrity of the aerogels in the mortars, both in the mixing process and the possible long-term chemical degradation, was a main concern. Finally, a preliminary test of the performance against fire spalling was performed. While aerogel-containing mortars were able to protect HPC cubes from fire spalling under a specific thermal loading protocol, the thermal conductivity and the mechanical properties obtained were similar to those of cellular concrete in the same range of total porosity. A possible explanation of the lower-than-expected insulation performance is the partial degradation of the aerogel filler by reaction with the alkaline pore solution of the mortars. Implications of these new findings on aerogel-cement mixtures are also discussed.

Keywords: tunnel; fire spalling; aerogel cement mortar; high-performance concrete.

1. Introduction

The numerous catastrophic tunnel fire events that have occurred during the past decades, e.g. the St. Gotthard fire (2001) in Switzerland and the Mont-Blanc Tunnel fire (1999) in France-Italy [1, 2], have increased the interest in structural fire safety of large underground facilities and have highlighted the importance of increasing the fire resistance in materials and structural design of tunnels. Tunnel fires are characterized by high peak temperatures, rapid heating rates, long durations and non-uniform temperature distributions within the tunnel. The temperature gradient over the cross section of the tunnel linings induces large stresses due to differential thermal expansion [3, 4]. At the same time, heating of the concrete causes evaporation of capillary and gel water and, in particular starting at about 200-250 °C, dehydration of the cement paste, which leads to shrinkage and progressive degradation of the matrix [3, 5]. The pressure of the water vapor confined in the pores of the cement paste increases with the temperature. While in conventional concrete the relatively high porosity of the matrix allows this pore pressure to dissipate, this is not the case for high-performance concrete (HPC) with low water-to-cement ratio (w/c) and very low porosity and permeability [6, 7]. As a consequence, HPC has been shown to be prone to explosive spalling when combinations of thermal stresses, pore pressure and external loads locally exceed the tensile strength of the concrete [3].

In recent years, intensive research has been dedicated to develop effective methods to limit or even prevent concrete thermal spalling by material design. Steel-fiber reinforced concrete [8] has been reported to have good resistance to high temperatures, possibly by limiting the propagation of macroscopic cracks. The most successful strategy is based on the addition of synthetic (mostly polypropylene, PP) fibers, alone or in combination with other admixtures such as air-entraining agents or superabsorbent polymers [9-12]. This approach is based on the fact that, upon melting of the PP-fibers, empty channels are created through which the water vapor escapes before high pressures can build up. The combination of fibers of different nature (e.g., steel and PP-fibers [13]) was also effective.

However, while such strategies may delay or avoid fire spalling and improve the structural behavior during fire, they lead to serious degradation of the main structure of the tunnel, which needs often to be rebuilt even if the fire has been brought under control after a short period.

On the other hand, a protective layer that can efficiently insulate the structural concrete and delay the temperature increase during fire may constitute a valid alternative to prevent explosive spalling. This approach would also allow to maintain the structural performance of the main concrete shield structure and to avoid or reduce costly repair, especially in the case when the tunnel fire can be rapidly brought under control. Obviously, the material for the insulation layer needs to possess high thermal resistance and stability at high temperatures, since in many applications it will need to be applied only in relatively thin layers (typically, a couple of cm at most). Some studies describe the use of thermal barriers to protect the concrete. However, with the limited thickness (40-80 mm) that is compatible with clearances in a tunnel, the insulating performance of some commercial products was found to be insufficient and the underlying concrete is protected only for about 40-130 mins under fire conditions.[14] On the other hand, in Terrasi et al. [15] a 10-mm thick mineral fire protection coating (a commercial spray-coated cement-bonded glimmer mortar) applied onto the whole fire-exposed concrete surface was effective in increasing the fire resistance of a 45 mm-thick HPC slab prestressed with tendons made of carbon-fiber-reinforced polymer. Klingsch et al. [16] applied different thicknesses (10 to 50 mm) of two different commercial lightweight protective mortars to HPC slabs. Both protective mortars were effective in avoiding fire spalling for 120 minutes of exposure to an ISO fire [17], except for one case with the minimum thickness of the mortar layer. Similar results were obtained later also by Lu [18], in whose experiments with a mortar layer of 10 mm thickness, spalling was only delayed and it was more violent and deeper reaching than for the unprotected concrete. From these results, it is clear that there is scope for improving the properties of insulating mortars used for fire protection.

Aerogels are a class of materials with ideal thermal insulation properties. Due to their mesoporous network structure, the gas conductivity is strongly suppressed by the Knudsen effect, leading to record-low total thermal conductivity values, typically in the range of 0.013 - 0.020 $W \cdot m^{-1} \cdot K^{-1}$ at 25°C and atmospheric pressure [19]. Aerogels can be made from silica [20-25], carbon [26-29], different organic materials [30-32] or organic-inorganic composites .[33, 34] Among them, silica-based aerogels are characterized both by good temperature resistance [35-37] and a straightforward fabrication process [38-40].

Aerogel-based cementitious composites have been the object of growing interest in the last few years. Ratke [41] was the first to report a concrete composite loaded with 70 vol. % silica aerogel granules that showed excellent fire resistance. In particular, an aerogel concrete plate with 50-mm thickness was able to maintain a temperature below 60 °C on the cold side upon exposure of the opposite side to a fire at 1000 °C for 2h [41]. Gao et al. [42] described an aerogel concrete with 60 vol. % aerogel granulate loading, displaying an average compressive strength of 8.3 MPa and thermal conductivity of 0.36 W $m^{-1}K^{-1}$. In the same study, the authors further observed that the air void content was close to zero in these aerogel containing mortars.

One main concern when incorporating silica-based aerogels into a Portland cement mortar is the possible chemical dissolution of the silica aerogels by the pore solution. The pore solution has a pH > 13 and is well-known to dissolve all types of silica, for example in the alkali-silica reaction that causes expansion of aggregates and cracking of concrete [43-45] or in the pozzolanic reaction of silica fume [46, 47]. In principle, silica aerogels, due to their very high surface area, are expected to be particularly reactive and may be partially or totally dissolved upon contact with the pore solution. However, according to Gao et al. [48], aerogels were found to be stable in Portland cement composites when silica fume was added to the mixture, presumably because the silica fume was acting as a sacrificial filler and was reacting before the hydrophobic and thus somewhat better protected aerogel phase. However, if the internal structure of the aerogels is degraded or partially dissolved by reaction with the pore solution, aerogel particles may partially collapse, lose some of their insulating properties and allow further gas conduction losses through the resulting gap between the cement matrix wall and the partially collapsed aerogel particle. From the literature, different strategies are known to reduce the pH-value of the pore solution, for example addition of silica fume [49] or utilization of less alkaline cementitious binder systems, for example calcium sulfoaluminate binders [50, 51]. However, it remains still unclear what level of alkalinity is tolerated (both, short and long-term) by the aerogel fillers under real application conditions. Aerogels composites with weakly alkaline binders such as gypsum mortars have also been reported [52], however those are not suitable for direct contact with HPC in the presently envisaged application (see, e.g., [53]).

In this work, we suggest a simple approach to avoid or limit explosive spalling of shield concrete in a tunnel by decorating the surface of HPC structural elements with aerogel-cement mortars. Aerogel mortars are a comparatively new class of materials, for which limited characterization is available in the literature and many open questions remain, e.g. about the short term (during mixing) and long-term (due to chemical stability in the pore solution) integrity of the aerogels. To allow a systematic design of these mortars for the intended applications, the microstructure, the pore structure, the thermal conductivity and mechanical properties of the mortars were studied in depth. In addition, a preliminary assessment about the performance of the aerogel mortars against fire spalling of HPC has been performed, covering only a limited number of samples with one type of aerogel mortar. The aerogel mortars studied in this paper are different from commercially-available lime-based renders,[54] which have higher aerogel content and are characterized by reduced alkalinity and extensive carbonation.

2. Materials

2.1. Materials and aerogel-cement mortar preparation

Mortars were prepared by a two-step mixing. First, dry cement, sand, silica fume and aerogel particles were mixed in a 1.75-l barrel. Then, a solution of water and superplasticizer was added and the mixture was further stirred until it became homogenous. The cement used in this study was a CEM I 52.5 R ordinary Portland cement (particle density: 3150 kg/m^3, Blaine fineness). Silica fume (particle density: 2200 kg/m^3) was added to increase the strength of the matrix. A superplasticizer (polycarboxylate ether, PCE) in liquid form was employed. An alluvial sand (particle density: ~ 2680 kg/m^3) was sieved to particle sizes 0.5–2 mm. Hydrophobic aerogel granules (P300, particle size 1.2-4 mm, particle density: 125 kg/m^3) were received from Cabot, Germany. De-ionized water was used.

The water–binder ratio (w/b) was set to 0.40, where the binder is the sum of cement and silica fume, whose content was 10 wt. % of the binder. The superplasticizer content was 1 % of the binder phase. While the volume of aggregates (sand + aerogel) was 67 vol. % for all mortars, the relative volume of sand and aerogel was varied systematically between the mixtures. In the calculation of the mix proportions, the air content was assumed to be 2 vol. % in the reference mortar without aerogels. For the aerogel mortars, following the observation in [42] (see introduction), the air content was assumed to be zero. The composition of the mortars (based on the density of the constituents and on the assumed air content) is reported in Table 2.

Table 2. Mix proportions of the mortars (g).

Sample code	Water	Cement	Silica fume	superplasticizer	Sand	Aerogel granule	Aerogel fraction (vol. %)
RefC	54.29	115.20	12.80	1.29	524.44	0	0
AeroC 1	54.29	115.20	12.80	1.29	262.22	12.24	33
AeroC 2	54.29	115.20	12.80	1.29	196.66	15.30	42
AeroC 3	54.29	115.20	12.80	1.29	131.11	18.63	50
AeroC 4	54.29	115.20	12.80	1.29	65.55	21.43	58
AeroC 5	54.29	115.20	12.80	1.29	0	24.49	67

Well-mixed slurries were poured into stainless steel prismatic molds (40 × 40 × 160 mm^3) to produce specimens for mechanical testing (bending strength and compressive strength) and a cylindrical plastic mold (Ø60 mm × 15 mm) for ambient thermal conductivity measurements. As prepared samples were kept sealed in their steel molds in a controlled atmosphere at 20 ± 0.3 °C and RH >95% before demolding. Subsequently, the samples were cured in the same atmosphere for either 7 days or 28 days. For each composition, three identical samples were prepared and characterized.

2.2 Preparation of high-performance concrete cubes coated with aerogel mortars

To allow a preliminary evaluation of the effect of aerogel mortars on the explosive thermal spalling of HPC, five 150 × 150 × 150 mm^3 cubes were prepared for one-side thermal loading. After casting, the HPC samples (see Table 3 for the mix composition) were kept at >95% RH and 20±0.3 °C. This HPC composition was chosen because it systematically spalled in previous studies with the same heating regime. At the age of 1 day, the samples were demolded and stored in a >95% RH and 20±0.3 °C climatic room. At the age of 140 days, four HPC cubes were coated with the AeroC 3 mortar (see Table 2 for the mix labels). Mortar layers of 13, 18, 42 and 48 mm thickness were applied onto one face of the concrete cubes; these layers correspond to a layer of minimum thickness (which resulted on average 13 or 18 mm on two distinct cubes) and a layer of about twice the minimum thickness (42 or 48 mm on average on two cubes). Before performing the thermal spalling tests, the samples were cured in a >95% RH and 20 ± 0.3 °C climatic room for 7 days, then they were moved to a 70% RH and 20 ± 0.3 °C climatic room for 3 days.

Table 3. Mix composition of HPC [kg/m^3]

Cement CEM I 52.5 R	488
Silica fume	122
Aggregate 0-4 mm	1582
Superplasticizer	8.54
Water	189.1
w/b	0.31

Before the one-side thermal loading, the samples were insulated with high-temperature resistant aluminum tape (3M High Temperature Aluminum Foil Tape 433) from four sides and the top surface to prevent vapor loss and facilitate explosive spalling. Due to the moisture sealing of the lateral surfaces with high-temperature resistant aluminum tape, the cubes behave similarly to samples with larger dimensions in the direction perpendicular to the heating direction. The same HPC mix design and vapor insulation were used in a number of studies on moisture movement in concrete due to one-side thermal loading [55-58]. The sides of the cubes were in addition thermally insulated with 20 mm-thick layers of foamed glass.

3. Methods

3.1 Measurements of density

The solid skeleton density was obtained from the skeleton volume, determined by helium pycnometry (AccuPyc II 1340, Micromeritics, US). The bulk densities were determined from the mass and volume measured by powder pycnometry (Micromeritics, GeoPyc 1360) with a low confining force of 4 N (corresponding to ~35 kPa) to reduce excessive compression of the (weak) aerogels during the measurement.

In addition, a second, independent estimation of the bulk density was obtained by measuring the mass of the prismatic specimens ($40 \times 40 \times 160\ \mathrm{mm}^3$) immediately before the strength measurements (see section 3.5).

3.2 X-ray micro-tomography

X-ray micro-tomography was performed at the Center for X-ray Analytics at Empa with a custom-developed instrument consisting of a Perkin Elmer XRD 1621 CN2 ES® flat panel X-ray detector (Perkin Elmer), with 2048 × 2048 pixels of physical size p = 200 μm and a VISCOM XT9160 TXD X-ray source (Viscom AG), based upon a 6 μm-thick tungsten target and a minimum focal spot size of a few μm for the electron beam.

The X-ray source voltage and current were 90 kV and 110 μA, respectively. The tomographic measurement consisted in acquiring 2401 radiographs at different sample orientation angles between 0° and 360°. The geometrical magnification factor, M, of the micro-tomography measurement depends upon the source-to-detector distance, d_{SD}, and the source-to-specimen distance, d_{Ss}, according to the equation $M = \frac{d_{SD}}{d_{Ss}}$. In our case, d_{SD} = 1017 mm, d_{Ss}= 36.5 mm, thus $M \cong 27.86$, leading to an effective pixel size for the radiographs and effective voxel size for the tomogram $\tilde{p} = \frac{p}{M} \cong 7.2$ μm (this value varied slightly among the different samples).

Any kind of tomographic imaging method produces 3D images, usually called tomograms. Depending on the type of physical radiation used for performing tomography, the tomogram is a 3D spatial distribution of a physical variable (in short, a scalar field). In the case of standard X-ray tomography (also called X-ray attenuation-contrast tomography, used in this work), the scalar field is the X-ray attenuation coefficient μ of the specimen, which is directly proportional to the volumetric mass density, ρ, and to a power of the effective atomic number, Z_{eff}^{n}, with n being typically a number between 3 and 4 [59].

Any kind of tomogram is not a direct image, meaning the direct output of the measurement process itself. It is rather the results of a mathematical reconstruction, obtained with a tomographic reconstruction algorithm, starting from a set of raw, direct images. Such images are 2D, projection images, usually called radiographs and acquired at distinct angles, within 360°, of orientation of the specimen around its vertical axis. From such set of projection at distinct angles, Fourier transform of the scalar field can be estimated, thus the actual scalar field can be finally sampled (or "reconstructed") [59].

In our specific case, the tomographic reconstruction from the set of 2401 radiographs was performed with the implementation of state-of-the-art cone beam filtered back-projection algorithm [60] in the Octopus Reconstruction software by XRE (https://xre.be). Such algorithm was run with standard settings, without special pre-processing of the radiographs, e.g., without need of correction for beam hardening-induced artifacts.

3.3 Scanning Electron Microscopy

A sample of aerogel mortar AeroC 3 was dried in an oven for 3 days at 50 °C. Afterwards, it was impregnated with epoxy resin in vacuum (without applying external pressure, to preserve the structure of the aerogels), cut, polished and carbon coated. A ThermoFisher Scientific/FEI Nova NanoSEM 230 in high vacuum mode was used for imaging (3.0-5.0×10^{-6} Torr) with an acceleration voltage of 12 kV, a spot size of 4.5 and a beam current of 210-240 µA. A Qxford

SSD detector (80 mm^2) and INCA Energy software with ZAF correction were used for energy dispersive X-ray spectroscopy (EDS) analysis.

3.4 Brunauer-Emmett-Teller (BET) specific surface area.

N_2-sorption BET analysis is commonly used to estimate the surface area and to characterize the pore structure of porous materials. It probes the interaction between a gas, e.g., N_2, and an adsorbent and it can measure specific surface areas down to 0.01 m^2 g^{-1} and pore diameters in the range of 0.3 to 100 nm [61]. When applied to mortars with varying aerogel contents but constant cement paste volume, the BET surface area is expected to correlate with the amount of aerogels in the mortars. In addition, the BET surface area measurements are also employed here to verify whether the pore structure of the aerogels in the mortars is intact. Nitrogen adsorption and desorption isotherms at – 196°C were measured on an ASAP 2020c instrument (Micromeritics, USA) with 10 s equilibration time. The specific surface area of the samples was determined by using the Brunauer–Emmett–Teller (BET) theory employing the range between 0.0 and 0.3 relative equilibrium pressure p/p_0, p being the applied pressure and p_0 the N_2 condensation pressure at the measurement's temperature.

3.5 Bending and compressive strength

Bending strength and compressive strength of the aerogel mortars were determined for 15 and 31 day aged specimens, except for AeroC 4 and AeroC 5, where, due to logistics, the first measurement age was moved up in the schedule to 10 and 7 days, respectively.

While the bending strength was measured on three prismatic samples (40 × 40 × 160 mm^3) at each age, the compressive strength was measured on the six half-prisms that resulted from the bending tests. The procedure for strength measurements was based on the European standard EN 196-1.

3.6 Thermal conductivity

The thermal conductivity was measured on 2 different devices: the smaller cylindrical aerogel-cement mortar samples (Ø60 mm × 15 mm) were measured on a custom-built guarded hot plate device (guarded zone: 50 × 50 mm^2, measuring zone: 25 ×25 mm^2) with a 15 °C temperature difference, which was originally designed for small samples of low thermal conductivity materials [54]. In order to be consistent with measurements according to the European Standards EN 12667, calibration measurements were carried out using conventional expanded polystyrene samples measured once in a 500 × 500 mm^2 calibrated and validated testing equipment. The small guarded hot plate measurement data was then calibrated using these known standards. Note that a high measurement uncertainty (20%) is expected for the aerogel-cement mortar samples with relatively high thermal conductivity in the range of 0.1-1.0 W/(m K).

The plain concrete sample (250 × 250 × 50 mm^3) was recorded on a heat flow meter (HFM) according to ISO 8301: 1991, with 3% uncertainty. In this case, the small uncertainty is due to the precise surface temperature measurement of the attached thermocouples on the surface of the sample.

3.7 Evaluation of explosive spalling

Thermal loading was performed from one side of the specimens (corresponding to the side coated with aerogel mortar, except for the case of the reference, uncoated HPC) using a heating plate [62]. The heating process started from room temperature and the temperature of the plate was increased uniformly up to a maximum temperature of 600 °C within about 40 minutes. The maximum temperature was kept for 2 hours, followed by free cooling down on the heating plate in ambient air. The outcome of this test was evaluated only qualitatively, as either “spalling” or “no spalling”.

The aim of the high-temperature spalling tests was to give a preliminary assessment of the potential of these aerogel mortars to protect concrete from spalling during high temperature exposure. While both the maximum temperature reached and the heating rate are lower than might be encountered at the surface of concrete directly exposed to tunnel fires, at a certain distance from the fire there will be locations where the surface will heat up at slower rate and reach lower final temperatures.

4. Results and discussion

4.1. Distribution of aerogel granules and macroporosity of mortars

The aerogel granules could be easily mixed with cement before and after adding water, which is consistent with reports in the literature (e.g., [42]). To assess whether the aerogel particles remained intact during mortar mixing and whether they were homogenously distributed in the hardened mortars, X-ray micro-tomography was employed (results shown in Figs. 1 and 2).

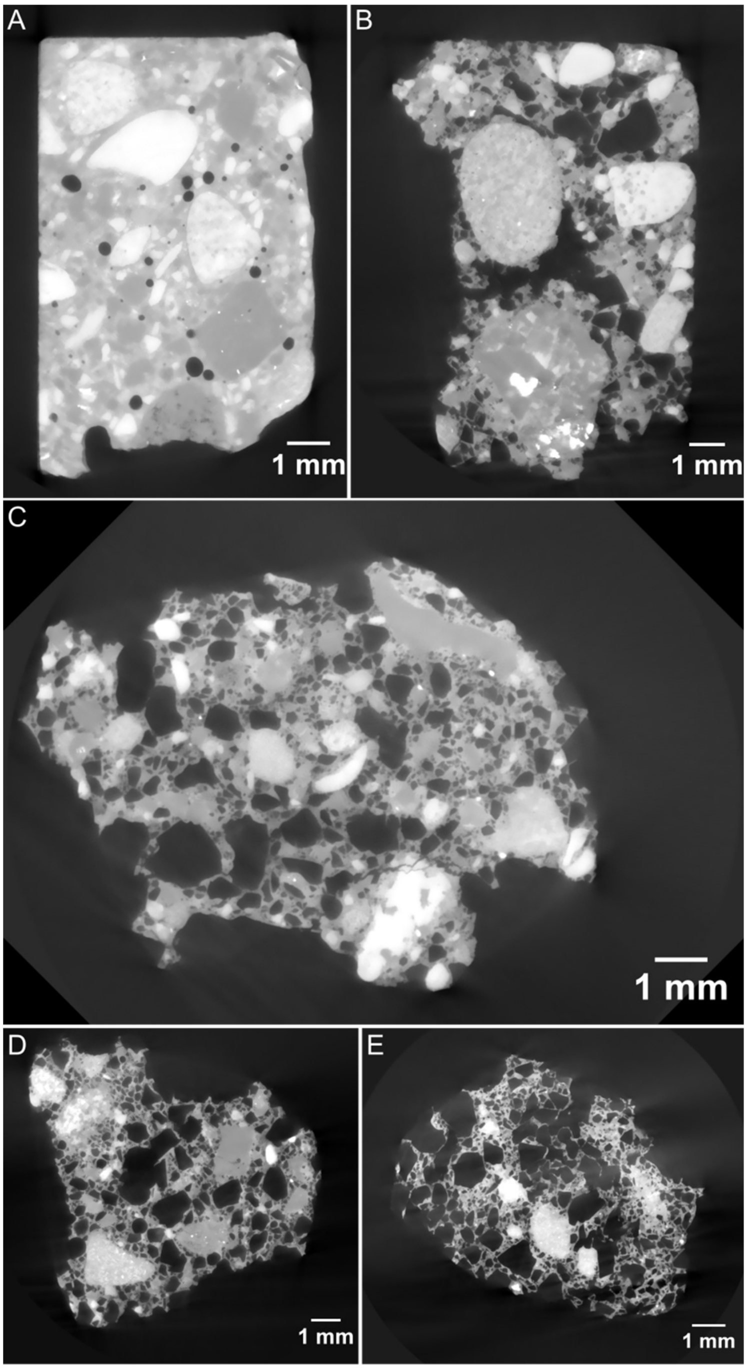

Figure 1. 2D digital cross-sections (ortho-slices) from the X-ray tomogram (3D image) of each aerogel mortar specimen. a) reference mortar, without aerogel granules; b) AeroC 1; c) AeroC 2; d) AeroC 3; e) AeroC 4. Voxel size = 6.7 µm, 7.8 µm, 6.9 µm, 7.3 µm and 6.2 µm for the respective specimens.

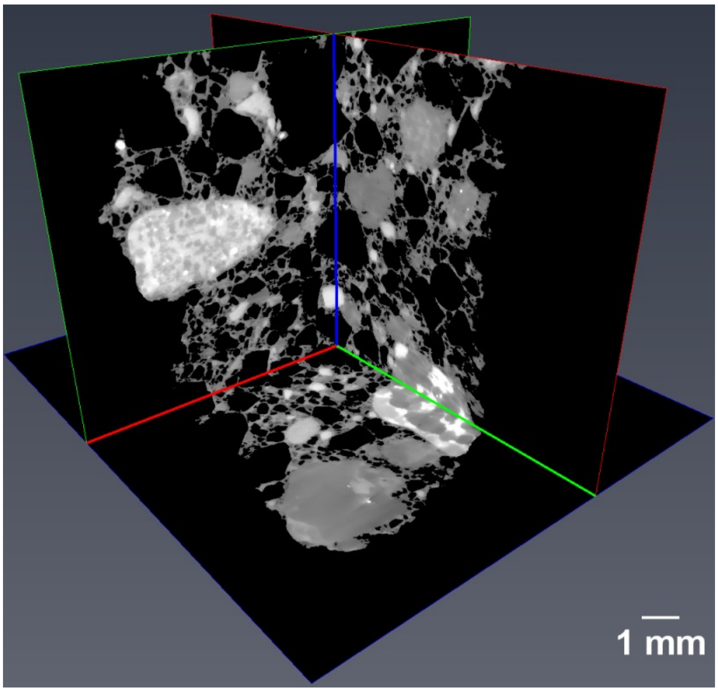

Figure 2. Mutually orthogonal 2D digital cross-sections (slices) of the X-ray tomogram of the AeroC3 specimen.

Figure 1, parts *a* to *e*, shows 2D digital cross-sections (slices) of the X-ray tomograms of aerogel mortar specimens with different amounts of aerogels (see Table 2 for the mixture compositions). The voxel value in such tomograms (3D images) is positively correlated with the X-ray linear attenuation coefficient, which itself is directly proportional to the electron density n_e and to a power of the atomic number Z. Brighter voxel values in the images in Fig. 1 mean higher X-ray attenuation due either to higher local density or to the presence of higher Z elements or to a combination of the two.

The increasing volume of aerogels incorporated into the mortars is clearly visible already in the tomographic slices. Figure 2 shows three mutually-orthogonal slices of the X-ray tomogram of an AeroC3 specimen, the same from which the slice in Fig. 1D was obtained. In this 3D view, the spatial distribution of pores, large and small, is even more evident, pointing to a cellular-/foam-like structure of the specimen at that particular aerogel loading. While the porosity varied considerably over the different regions within the examined samples, the global macroporosity (comprising aerogel particles and air voids), as estimated from the 3D image analysis of the X-ray tomograms, was found to be in most cases in good agreement with the theoretical values calculated on the basis of the mixture compositions of the mortars (see Table 4). The differences, never larger than 5% absolute porosity, may be due to the observed inhomogenous distribution of the aerogel particles within the small mortar volumes that were measured by X-ray micro-tomography. A better agreement, albeit at the cost of spatial resolution, may have been obtained by imaging larger mortar samples.

While the good agreement between the porosity of the mortars measured by X-ray micro-tomography and the calculated values shown in Table 4 indicates that no major crushing of the aerogels during mixing took place, some degree of fragmentation of the original aerogel granules cannot be excluded based on volumetric considerations alone.

Table 4. Calculated and measured macroporosities (including aerogel particles) of the aerogel mortars in % by volume of the whole mortar.

Sample	Calculated	Tomography
RefC	2.0[1]	2.6
AeroC 1	33.3	33.6
AeroC 2	41.7	36.7
AeroC 3	50.4	43.7
AeroC 4	58.3	57.5
AeroC 5	66.7	N.A.

[1] 2 vol. % of air voids was assumed only for RefC

4.2. Density of the aerogel mortars

The density of the mortars, measured both by pycnometry and by mass and volume measurements on macroscopic samples (see Section 3.1), is shown together with calculations based on the mixture compositions of the mortars. The density values obtained from the bulk samples are within 1.5% of the densities calculated based on the mixture compositions, except for AeroC 5 where the calculated density is about 4% lower. The calculations assume that the mortars with aerogels contained no large air voids (see [42]) and they do not take into account that the mortars were cured in a room at high RH and may have experienced limited mass (i.e. moisture) uptake during curing. The results from pycnometry were almost always higher and generally suffered from higher scatter, possibly due to the small sample sizes that were examined.

Table 5. Calculated (based on mix composition, see Table 1) and measured densities of the aerogel mortars in kg/m^3. The values between brackets are the standard deviations (when applicable).

Sample	Calculated	Bulk samples	Pycnometry
RefC	2315[1]	2288(7)	2317(32)
AeroC 1	1559	1555(11)	1638(44)
AeroC 2	1347	1339(17)	1512(25)
AeroC 3	1126	1140(20)	1086(3)
AeroC 4	920	926(30)	945(49)
AeroC 5	707	737(26)	768(50)

[1] 2% of air was assumed only for RefC

4.3. SEM investigation

The microstructure of the aerogel mortar was investigated by SEM analysis. A typical sample (AeroC 3) clearly shows aerogel particles embedded in the cement paste matrix (Fig. 3). The individual aerogel particles are clearly distinguishable from both, the cement paste and the cavities (filled with epoxy after impregnation), which appear between the aerogel particles and the cementitious paste. Along the walls of the voids, single or multiple layers of reaction product material are recognizable. Typically, different layers at the interface between aerogel particle and cement matrix are clearly identified and show some variation in the backscatter intensity in SEM (which is related to atomic number and density). The backscatter intensity is higher in direct contact to the cement paste and on the inner side of the wall, suggesting at least a partial dissolution of the original silica aerogel (Fig. 4). This is further supported by the presence of dark voids (filled with epoxy), where presumably the silica aerogel has been completely dissolved. EDX analysis performed on the interfacial region indeed shows that the silica of the aerogel particle reacted with the pore solution of the mortar, forming a low Ca/Si-ratio calcium-silicate-hydrate (C-S-H) interfacial layer, with aluminum and alkalis as minor constituents. The increased backscattering intensity is the result of an increased atomic Ca/Si-ratio (Fig. 5).

Fig. 6 shows a zoom on a different reactive interface where two distinct morphologies are visible, in particular a dense C-S-H gel layer and a rather porous structure. This latter structure may stem from a partially collapsed aerogel layer, which may have delaminated from its parent particle or the rest of the parent particle may have been lost during SEM sample preparation. By examining the preserved structure of this porous reaction product layer, the ubiquitous presence of calcium confirms the reaction between the original silica aerogel and the mortar's pore solution (Fig. 7). However, the extent of the reaction varies from particle to particle and also locally and hence cannot be quantified in this work.

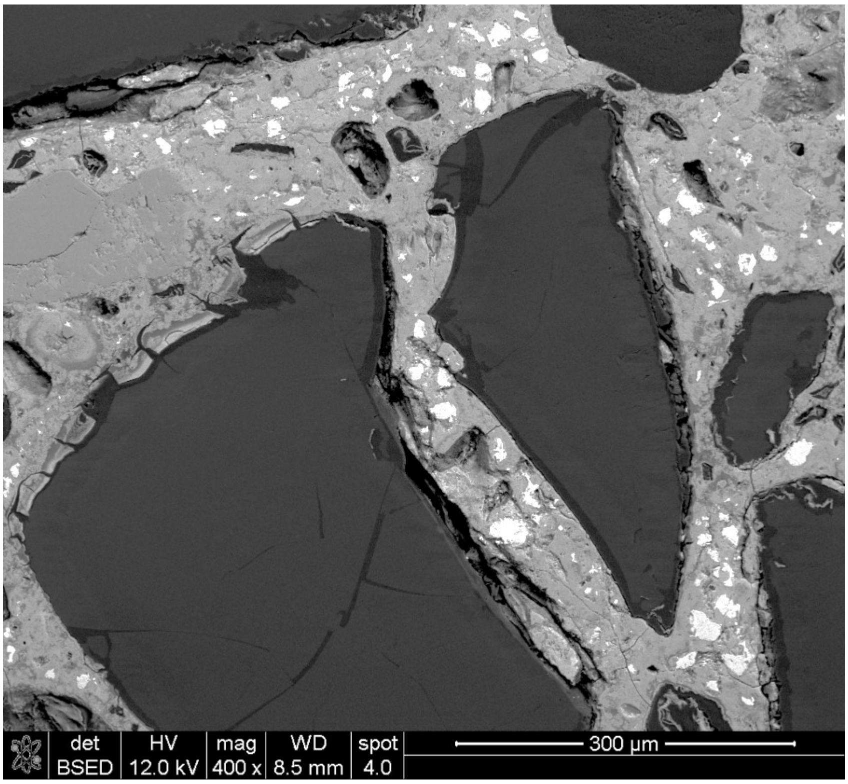

Figure 3. Microstructure of the AeroC 3 sample imaged by BSE-SEM, in which the aerogel particles are recognizable as darker gray inclusions embedded in the cement paste (lighter shade of gray, with unhydrated cement in white).

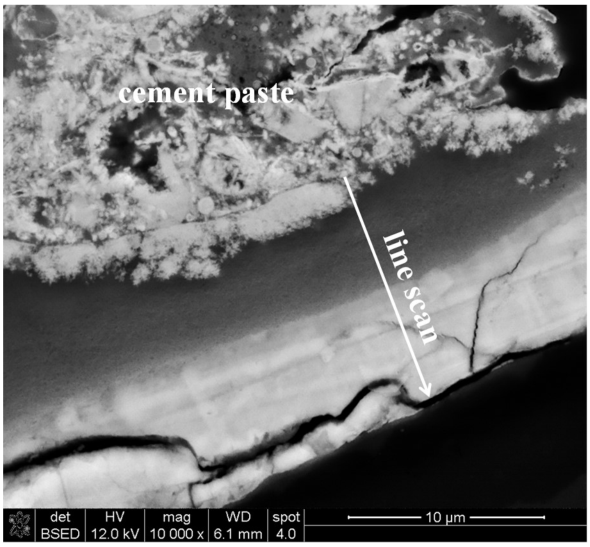

Figure 4. Interface between aerogel particle and cement paste observed in the AeroC 3 sample. The marked EDX line scan marks the thickness of the reacted product phase. The data are presented in Figure 5.

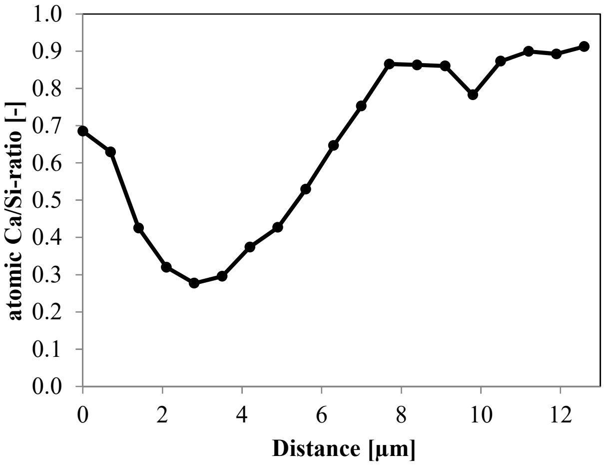

Figure 5. Ca/Si-ratio across a reacted product phase in the AeroC 3 sample representing the interface between the aerogel particle and the cement paste, as indicated in Figure 4. Contact to the cement paste is at a distance of zero.

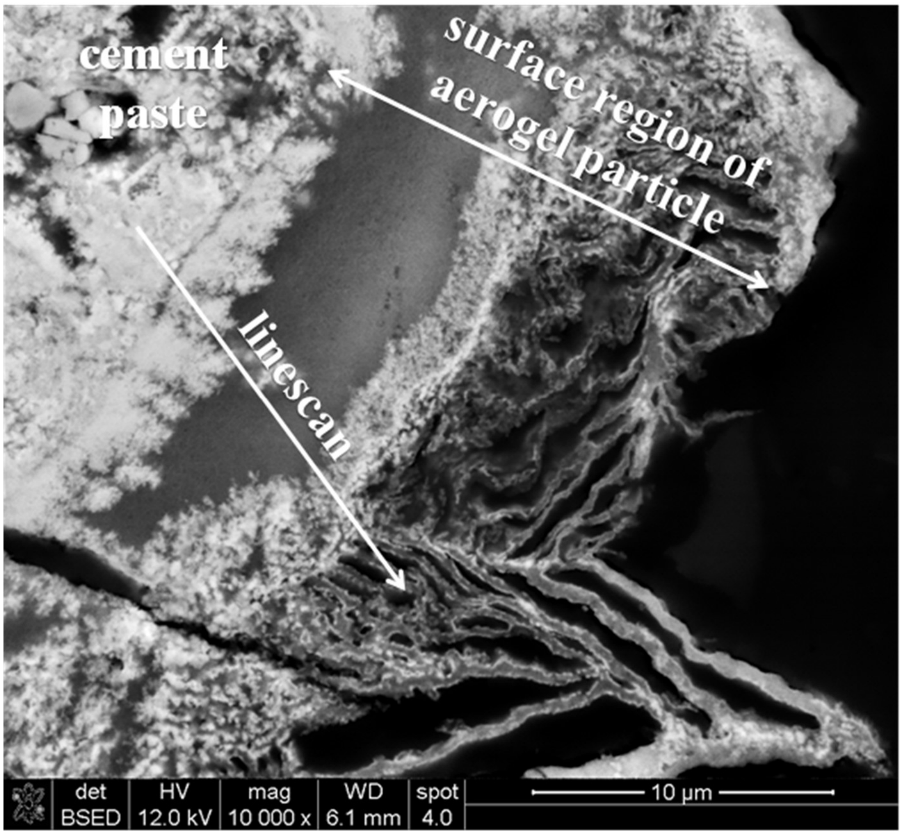

Figure 6. SEM image in the AeroC 3 sample showing a multilayer C-S-H reaction product phase stemming from the partial dissolution of an aerogel particle with dense and porous layers. The marked EDX line scan is presented in Figure 7.

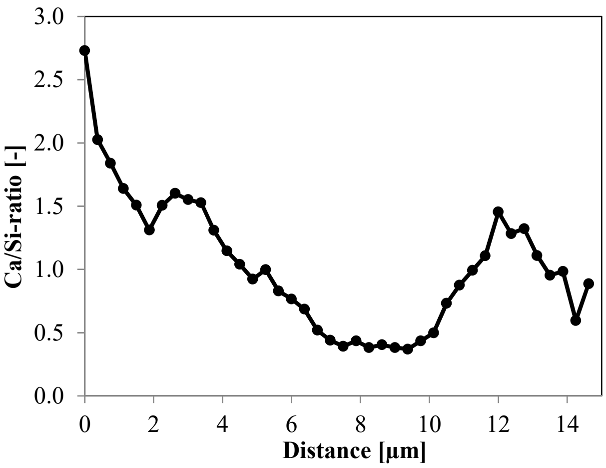

Figure 7. Ca/Si-ratio from the cement paste (left up to a distance of 2 µm) across the multilayer reaction product phase in the AeroC 3 sample. The location of the scan is indicated in Figure 6.

The results presented in Figures 3-7 suggest that the silica aerogel particles are partially dissolving in the alkaline environment provided by the hydration of the cement clinker in the mortar. The reaction between the pore solution and the aerogel particles leads to the formation of C-S-H with a generally low Ca/Si-ratio, ranging from 0.3 to 1.6. Higher Ca/Si-ratios in the reaction product layer (Figure 6) were observed in direct contact with the cement paste. However, calcium was also present in the porous reaction product layer further away from the interface. As a result of the chemical reaction between silica and pore solution, part of the mesoporous silica aerogel phase seems to convert to Ca/Si gel.

4.4 BET specific surface area

The specific surface area obtained from BET is displayed in Figure 8, in which the average values and the standard deviation of two measurements are shown. While the scatter of the measurements is high, it is remarked that the highest values for both volume and surface area were found in the mortars with the highest amounts of aerogel. If one supposes that the aerogel phase and with it the surface area of the aerogels (measured separately as 720 m^2/g) were to remain completely intact in the mortar samples (neglecting the reaction with the pore solution that was discussed above) and that the sand has negligible contribution to the BET surface, one can estimate the BET surface area of the mortars as a weighted average of the surface area of the aerogel and the cement paste, respectively (see dashed line in Figure 8). For this calculation, the contribution of the cement paste was obtained based on the experimental results of the reference mortar without aerogels as 15 m^2/g, which is within the range of values reported for Portland cement pastes [63, 64]. Albeit the BET surface area has been shown to vary widely depending on the porosity of cement pastes [65], the drying conditions and the measurement protocol [66, 67], in this case the aerogel phase is the main contributor to the measured surface area (compare the blue and the red line in Figure 8), despite the relatively small mass loadings. As evident from Figure 8, the calculated BET surface (dashed red line) matches the measured ones within the experimental error. Although the formation of a Ca/Si gel of high surface area [68] along the aerogel/cement paste interface could affect the results, its contribution to the surface area is expected to be minor. Indeed, the BET results confirm that the majority of the aerogel phase remains intact within the aerogel mortars examined in this study.

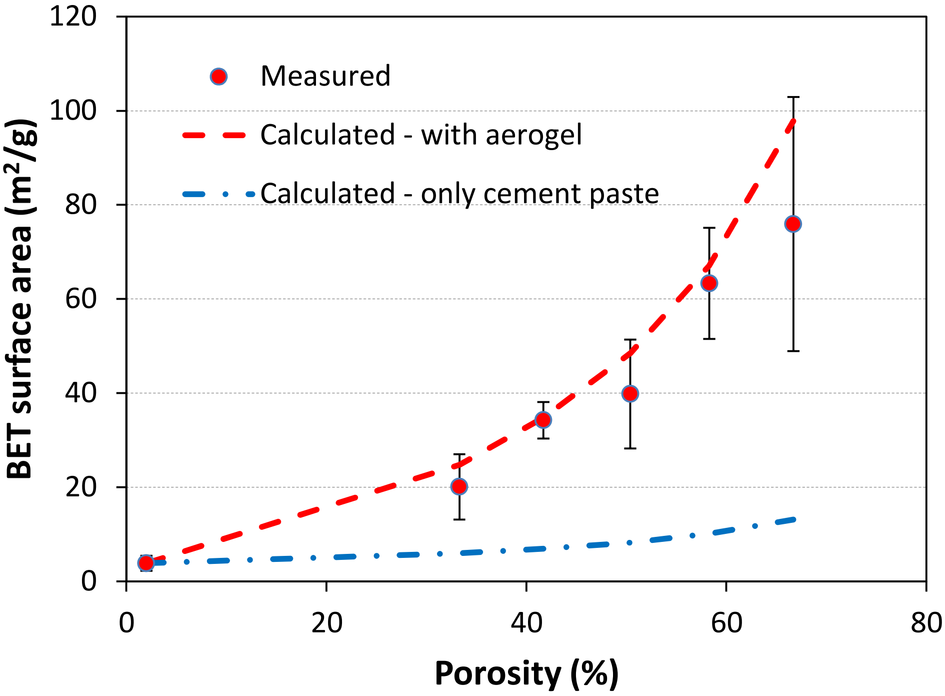

Figure 8. BET specific surface area of aerogel mortars with different amounts of silica aerogels, plotted against their calculated porosity (see Table 2). The data points show experiments with standard deviation from two repetitions, while the dashed red line shows calculations according to a mixture rule (see text for details). The lower blue line shows the contribution of the cement paste only.

4.5. Mechanical properties of the aerogel mortars

All the flexural and compressive strength results, including the respective different curing ages, are reported in Table 6. While some strength increase between 15 and 31 days was measured in the reference mortar, the effect of curing age becomes lower as the strength declines and the scatter increases with aerogel amount.

Figure 9 shows plots of the bending and compressive strength after 31 days curing as functions of the porosity (i.e., the sum of the air voids and the aerogel volume calculated from the mixture composition, see first column in Table 4). A good fit of both the flexural and the compressive strength (R2 of 0.985 and 0.994, respectively) can be obtained with the following simple relationship (originally by Balshin [69]), often applied for cementitious materials and in particular for cellular concrete (see e.g., [70-73]):

$$f(p) = f_0 \cdot (1-p)^n \qquad (1)$$

where f [MPa] is the strength, f_0 [MPa] is the strength at zero porosity (usually estimated by regression), p [-] is the porosity and n [-] is an exponent that is usually between 3 and 5 for cementitious materials. In this specific case, the best fit was found with $n_b = 3.2$ for the flexural strength and $n_c = 4.5$ for the compressive strength.

It is noted that the compressive strength of the aerogel mortars appears to be lower than that of cellular concretes of comparable density. For example, for a dry density of about 700 kg/m^3, comparable to that of AeroC 5, compressive strengths of 3.9-8.5 MPa are reported in [74]. At the other end, for a density of about 1550 kg/m^3, comparable to that of AeroC 1, compressive strengths around 23-24 MPa were measured in [75]. Bing et al. [76] achieved compressive strengths of 30 MPa and higher with foam volumes of at least 30% and densities between 1300 and 1500 kg/m^3 (which corresponds to the density range covering AeroC 2 and AeroC 1 in the present study).

Despite their very low strength compared to the reference concrete, and also lower strength than cellular concrete of similar density, the aerogel mortars show much better mechanical properties compared with the extremely brittle pure silica aerogel [77]. In the application targeted in this study, the mechanical properties of these mortars are considered to be sufficient for brushing or spraying applications of thermal insulation layers, while the stiffness and the strength of the shield tunnel structure is still guaranteed by the underlying HPC elements.

Table 6. Mechanical properties of the aerogel mortars tested at different curing ages. The values between brackets are the standard deviations.

Sample	Age (d)	Bending strength (MPa)	Compressive strength (MPa)
RefC	15	10.7(0.6)	91.9(1.6)
	31	11.2(0.5)	97.7(1.9)
AeroC 1	15	2.8(0.2)	11.1(0.3)
	31	3.0(0.1)	13.0(1.3)
AeroC 2	15	1.7(0.1)	6.3(0.4)
	31	1.9(0.3)	8.0(0.5)
AeroC 3	15	1.1(0.5)	4.0(0.3)
	31	1.5(0.5)	6.0(0.3)
AeroC 4	10	0.8(0.1)	1.6(0.2)
	31	0.9(0.1)	1.7(0.3)
AeroC 5	7	0.7(0.1)	1.5(0.1)
	31	0.6(0.2)	1.4(0.3)

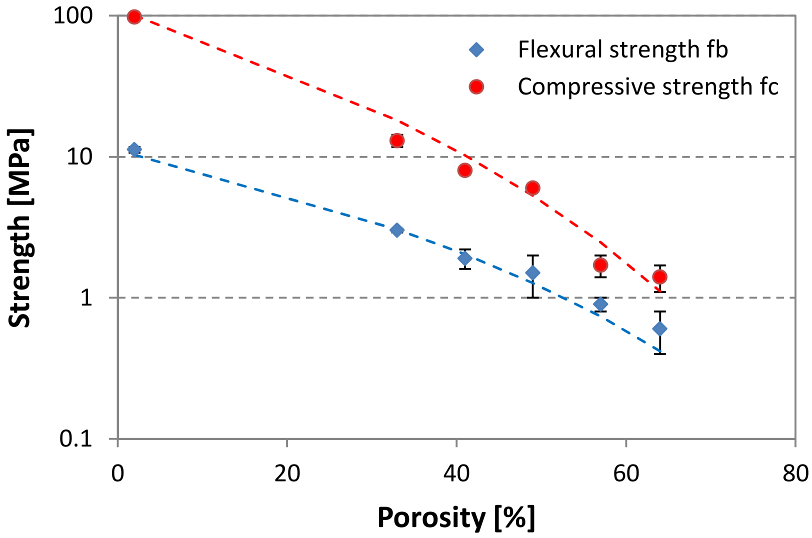

Figure 9. Flexural strength and compressive strength of the aerogel mortars after 31 days curing, plotted against porosity. Average values and standard deviations are shown.

4.6. Thermal properties of the aerogel mortars

Considering the suggested application for the developed mortars, namely avoiding or delaying spalling of HPC tunnel linings by delaying the temperature increase during exposure to fire, the thermal conductivity of the aerogel mortars is the essential parameter to control. RefC, without aerogels, had a thermal conductivity of 1.7 W/(m K), measured with a heat-flow meter. With the addition of 33 vol. % silica aerogels (Aero C1), the thermal conductivity shows a remarkable decrease to 0.4 W/(m K) (see Figure 10), which was separately measured with smaller specimens on a custom-built guarded hot plate device. With increasing amounts of aerogels in the mortar, a further, proportionally smaller decrease of thermal conductivity is observed. The aerogel mortar with 66.7 vol. % aerogel displays a thermal conductivity of 0.17 W/(m K). The thermal conductivity of the mortars was substantially reduced with increasing silica aerogel volume fractions in the mixture, but the value obtained at the highest volume fraction of aerogel is still very much higher than the thermal conductivity of the aerogel, ~ 0.012 W/(m K) [78]. This is clearly understandable considering that, especially at high aerogel loading, heat conduction will be dominated by the most conducting phase – the cement paste [79]. One convenient approach to calculate the thermal conductivity of cementitious materials based on their composition is by applying a Mori-Tanaka scheme [80], which homogenizes the thermal conductivities of the components (cement paste and aggregates):

$$\lambda_{eff}=\lambda_{paste}+\frac{3f_{agg}\lambda_{paste}(\lambda_{agg}-\lambda_{paste})}{3\lambda_{paste}+f_{paste}(\lambda_{agg}-\lambda_{paste})} \tag{2}$$

where λ_{eff} is the thermal conductivity of the cementitious material, λ_{paste} and λ_{agg} are the thermal conductivity of the cement paste and of the aggregates, respectively and f_{paste} and f_{agg} are their volume fractions. The Mori-Tanaka scheme in this form considers the mortar as a macro-isotropic composite with a continuous matrix (cement paste) that embeds isotropic spherical inclusions distributed homogeneously in the matrix.

Since Eq. 2 can be applied directly only to cases where the mortars contain one type of inclusions, it is used here for REF (containing only sand as inclusion) and AeroC 5 (containing only aerogel as inclusion). By assuming λ_{paste} = 0.9 – 1.0 W/(m K) (following [81], where it is shown that there is only a limited dependence on the w/c and the moisture content), $\lambda_{agg,sand}$ = 2.7 W/(m K) (value for quartz aggregates in [82]) and $\lambda_{agg,aerogel}$ = 0.012 W/(m K), one obtains λ_{eff} = 1.88 - 1.95 W/(m K) for REF and λ_{eff} = 0.23 - 0.26 W/(m K) for AeroC 5. Considering the uncertainties in the experimentally determined thermal conductivity of the components, these calculated values are rather close to the measured ones for the two mortars. In particular, the calculated value for AeroC 5 is in fact overestimating the experimentally measured one of 0.17 W/(m K) by 35-52%.

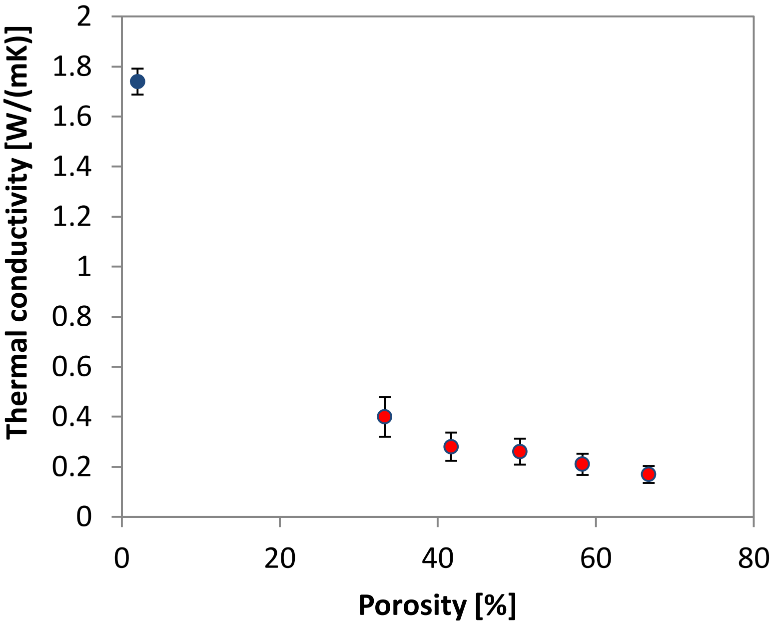

a)

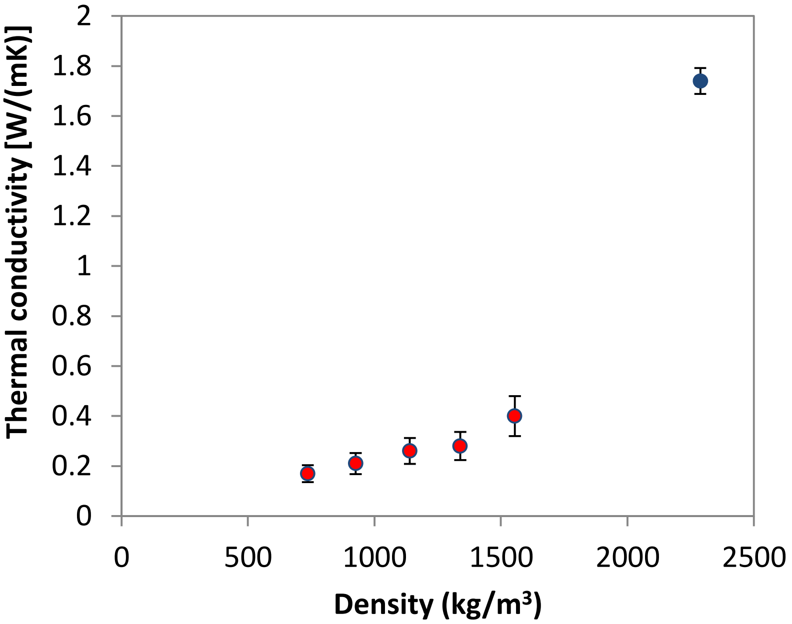

b)

Figure 9. Thermal conductivity of the aerogel mortars with various concentrations of silica aerogels, both as function of total porosity (a) and of density (b).

4.6 High-temperature spalling tests

This preliminary series of experiments was carried out on five samples, each consisting of a HPC cube with different thicknesses of the same AeroC 3 aerogel mortar applied to the heated side (including one cube without mortar lining). The HPC cube without mortar protection spalled after 25 minutes of thermal loading, confirming the susceptibility of this particular HPC to explosive spalling when exposed to high temperatures.[62, 83] In the case of the HPC samples protected by a mortar layer, explosive spalling occurred later on samples with 13 and 18 mm-thick layers (thinner mortar layer), at 68 and 148 minutes after the start of loading, respectively. On samples with thicker layers, namely 42 and 48 mm, spalling did not occur during the testing period (see Figure 10). It must be remarked here that these results are only preliminary, since they are based on only a limited number of experiments (two repetitions of the thinner layer and two repetitions of the thicker layer) with one type of aerogel mortar.

Figure 10. View of the heated surface of concrete cubes after the high-temperature spalling test. Left: sample without aerogel mortar, showing deep spalling. Right: sample with 48-mm thick aerogel mortar layer, without spalling.

Thermal insulation of constructions against fire is common practice but, in the case of existing tunnels and other structures where the space for thermal insulation is limited and effective thermal insulation is required, coating with an aerogel mortar may be able to delay heating of the

HPC and retard or avoid spalling. On the other hand, it has to be taken into account that for HPC samples with thinner mortar coating (on average either 13 or 18 mm), spalling was delayed but occurred deeper in the samples, with a correspondingly larger volume of spalled material. Similar results were reported with high temperature coatings (not containing aerogels) by Klingsch et al. [16] and by Lu [18].

While this preliminary spalling test showed that coating of HPC with an insulating mortar may be a promising route for delaying/avoiding spalling in HPC subjected to fire, these results need to be verified by studying a broader range of aerogel mortars and thicknesses of the coating layers. Furthermore, investigations are needed to assess the influence of different heating rates on the spalling behavior, in particular of higher heating rates and higher maximum temperatures that are typical for characteristic of surfaces directly exposed to fire. In addition, the issue of the integrity of the aerogels in the mortars should be first solved, to obtain mortars with lower thermal conductivity that can be applied in conveniently thin layers.

5. Conclusions

In this paper, a strategy for protecting tunnel shield high performance concrete (HPC) from explosive spalling was suggested, consisting in decorating the surface of HPC with aerogel-cement mortars of low thermal conductivity. While the aerogel granules appear homogeneously distributed in the cementitious matrix, their pore structure is altered at the cement/aerogel interface by the chemical reaction with the alkaline pore solution. For the different aerogel volume fractions in the mortars, the thermal conductivity was close to the range of expected values but also close to that of cellular concrete of comparable density. On the other hand, the compressive and bending strength of the aerogel mortars was lower than what is reported for cellular concretes of similar density. In a series of preliminary tests, layers of 40-50 mm of such aerogel mortars were able to prevent fire spalling of high-performance concrete cubes. It is remarked that further spalling tests need to be performed to cover a wider range of samples, materials and heating regimes.

Despite these preliminary encouraging results, the issue of partial reactive dissolution of hydrophobic silica aerogels and its impact on the long-term performance of these materials remains open. Although microscopy and BET results suggest that the majority of the aerogel phase remains intact, there is clear evidence of this reaction especially at the interface between cement paste and aerogels. Cementitious materials with lower pH, such as calcium sulfoaluminate cement, or binders that rapidly carbonate are expected to reduce the extent of aerogel dissolution. In principle, more robust aerogel chemistries could also show improved resistance against alkaline attack (e.g., methylsilane-based aerogels[84] etc.), although their practical use may be hindered by even higher cost and lack of commercial suppliers.

Acknowledgments

This work was financial supported by the National Natural Science Foundation of China (No. 51408073, 51678080 and 51678081). Part of this work was performed by the use of the Empa Platform for Image Analysis (http://empa.ch/web/s499/software-/-imaging-platform) at Empa’s Center for X-ray Analytics.

References

[1] B.A. Schrefler, P. Brunello, D. Gawin, C.E. Majorana, F. Pesavento, Concrete at high temperature with application to tunnel fire, Computational Mechanics 29(1) (2002) 43-51.
[2] A. Beard, R. Carvel, Handbook of Tunnel Fire Safety, Thomas Telford, London, 2005.
[3] G.A. Khoury, Effect of fire on concrete and concrete structures, Progress in Structural Engineering and Materials 2(4) (2000) 429-447.
[4] F. Lo Monte, R. Felicetti, Heated slabs under biaxial compressive loading: a test set-up for the assessment of concrete sensitivity to spalling, Mater. Struct. 50(4) (2017) 192.
[5] S. Mindess, J.F. Young, Concrete Prentice-Hall, Englewood Cliffs, NJ 481 (1981).
[6] P.-C. Aïtcin, High performance concrete, CRC press2011.
[7] E.W. Klingsch, A. Frangi, M. Fontana, High-And Ultrahigh-Performance Concrete: A Systematic Experimental Analysis on Spalling, Special Publication 279 (2011) 1-50.
[8] Z.-g. Yan, H.-h. Zhu, J.W. Ju, Behavior of reinforced concrete and steel fiber reinforced concrete shield TBM tunnel linings exposed to high temperatures, Construction and Building Materials 38(0) (2013) 610-618.
[9] P. Lura, G.P. Terrasi, Reduction of fire spalling in high-performance concrete by means of superabsorbent polymers and polypropylene fibers: Small scale fire tests of carbon fiber reinforced plastic-prestressed self-compacting concrete, Cem. Concr. Compos. 49(0) (2014) 36-42.

[10] D.J. Hannant, Durability of polypropylene fibers in portland cement-based composites: eighteen years of data, Cem. Concr. Res. 28(12) (1998) 1809-1817.
[11] P.C. Tatnall, Shortcrete in Fires: Effects of fibers on explosive spalling., Shortcrete (2002) 10-12.
[12] N. Segre, E. Tonella, I. Joekes, Evaluation of the Stability of Polypropylene Fibers in Environments Aggressive to Cement-Based Materials, Cem. Concr. Res. 28(1) (1998) 75-81.
[13] Z.-g. Yan, Y. Shen, H.-h. Zhu, X.-j. Li, Y. Lu, Experimental investigation of reinforced concrete and hybrid fibre reinforced concrete shield tunnel segments subjected to elevated temperature, Fire Safety Journal 71(0) (2015) 86-99.
[14] L. Boström, C.K. Larsen, Concrete for Tunnel Linings Exposed to Severe Fire Exposure, Fire Technology 42(4) (2006) 351-362.
[15] G.P. Terrasi, L. Bisby, M. Barbezat, C. Affolter, E. Hugi, Fire behavior of thin CFRP pretensioned high-strength concrete slabs, Journal of composites for construction 16(4) (2012) 381-394.
[16] E. Klingsch, A. Frangi, M. Fontana, Explosive spalling of concrete in fire. Test report 351, Institut für Baustatik und Konstruktion der ETH Zürich, 2013.
[17] ISO 834-1, Fire-resistance Tests: Elements of Building Construction-Part 1: General Requirements, International Organization for Standardization, International Organization for Standardization1999.
[18] F. Lu, On the prediction of concrete spalling under fire, Dissertation. ETH-Zürich. 2015. Nr. 23092. , 2015.
[19] M. Reim, W. Korner, J. Manara, S. Korder, M. Arduini Schuster, H.P. Ebert, J. Fricke, Silica aerogel granulate material for thermal insulation and daylighting, Sol. Energy 79(2) (2005) 131-139.
[20] X. Lu, P. Wang, D. Buttner, U. Heinemann, O. Nilsson, J. Kuhn, J. Fricke, Thermal transport in opacified monolithic silica aerogels, High Temperatures - High Pressures 23(4) (1991) 431-436.
[21] F. Ehrburger-Dolle, J. Dallamano, E. Elaloui, G.M. Pajonk, Relations between the texture of silica aerogels and their preparation, Journal of Non-Crystalline Solids 186 (1995) 9-17.
[22] S. Hæreid, E. Nilsen, M.A. Einarsrud, Subcritical drying of silica gels, Journal of Porous Materials 2(4) (1995) 315-324.
[23] A.V. Rao, P.B. Wagh, Preparation and characterization of hydrophobic silica aerogels, Materials Chemistry and Physics 53(1) (1998) 13-18.
[24] M. Schmidt, F. Schwertfeger, Applications for silica aerogel products, J. Non-Cryst. Solids 225(1) (1998) 364-368.
[25] D.M. Smith, A. Maskara, U. Boes, Aerogel-based thermal insulation, J. Non-Cryst. Solids 225(0) (1998) 254-259.
[26] N. Job, A. Thery, R. Pirard, J. Marien, L. Kocon, J.-N. Rouzaud, F. Beguin, J.-P. Pirard, Carbon aerogels, cryogels and xerogels: Influence of the drying method on the textural properties of porous carbon materials, Carbon 43(12) (2005) 2481-2494.
[27] D. Kawashima, T. Aihara, Y. Kobayashi, T. Kyotani, A. Tomita, Preparation of Mesoporous Carbon from Organic Polymer/Silica Nanocomposite, Chem. Mater. 12(11) (2000) 3397-3401.
[28] T. Kyotani, Control of pore structure in carbon, Carbon 38(2) (2000) 269-286.
[29] T. Yamamoto, T. Sugimoto, T. Suzuki, S.R. Mukai, H. Tamon, Preparation and characterization of carbon cryogel microspheres, Carbon 40(8) (2002) 1345-1351.
[30] X. Liu, M. Wang, W.M. Risen Jr, Polymer-attached functional inorganic-organic hybrid nano-composite aerogels, Materials Research Society, Boston, MA, United States, 2002, pp. 435-440.
[31] H. Tamon, H. Ishizaka, Preparation of organic mesoporous gel by supercritical/freeze drying, Drying Technology 17(7-8) (1999) 1653-1665.
[32] J.K. Lee, Oragnic aerogels reinforced with inorganic aerogel fillers, U.S., 2007.
[33] H.-B. Chen, B.-S. Chiou, Y.-Z. Wang, D.A. Schiraldi, Biodegradable Pectin/Clay Aerogels, ACS Appl. Mater. Interfaces 5(5) (2013) 1715-1721.
[34] L. Wang, D.A. Schiraldi, M. Sánchez-Soto, Foamlike xanthan gum/clay aerogel composites and tailoring properties by blending with agar, Ind. Eng. Chem. Res. 53(18) (2014) 7680-7687.
[35] J.E. Fesmire, Aerogel insulation systems for space launch applications, Cryogenics 46(2–3) (2006) 111-117.
[36] K. Ghazi Wakili, A. Remhof, Reaction of aerogel containing ceramic fibre insulation to fire exposure, Fire and Materials 41(1) (2017) 29-39.
[37] G. Wei, L. Wang, C. Xu, X. Du, Y. Yang, Thermal conductivity investigations of granular and powdered silica aerogels at different temperatures and pressures, Energy and Buildings 118 (2016) 226-231.
[38] M.M. Koebel, L. Huber, S. Zhao, W.J. Malfait, Breakthroughs in cost-effective, scalable production of superinsulating, ambient-dried silica aerogel and silica-biopolymer hybrid aerogels: from laboratory to pilot scale, J. Sol-Gel Sci. Technol. 79(2) (2016) 308-318.
[39] L. Huber, S. Zhao, W.J. Malfait, S. Vares, M.M. Koebel, Fast and Minimal-Solvent Production of Superinsulating Silica Aerogel Granulate, Angew. Chem. Int. Ed. 56(17) (2017) 4753-4756.
[40] J.F. Poco, P.R. Coronado, R.W. Pekala, L.W. Hrubesh, Rapid supercritical extraction process for the production of silica aerogels, Materials Research Society Symposium - Proceedings, 1996, pp. 297-302.
[41] L. Ratke, Herstellung und Eigenschaften eines neuen Leichtbetons: Aerogelbeton, Beton- und Stahlbetonbau

103(4) (2008) 236-243.
[42] T. Gao, B.P. Jelle, A. Gustavsen, S. Jacobsen, Aerogel-incorporated concrete: An experimental study, Construction and Building Materials 52(0) (2014) 130-136.
[43] D.W. Hobbs, Alkali-silica reaction in concrete.
[44] L.D. Glasser, N. Kataoka, The chemistry of 'alkali-aggregate'reaction, Cem. Concr. Res. 11(1) (1981) 1-9.
[45] A. Leemann, G. Le Saout, F. Winnefeld, D. Rentsch, B. Lothenbach, Alkali–silica reaction: the influence of calcium on silica dissolution and the formation of reaction products, J. Am. Ceram. Soc. 94(4) (2011) 1243-1249.
[46] P. Mehta, O. Gjørv, Properties of portland cement concrete containing fly ash and condensed silica-fume, Cem. Concr. Res. 12(5) (1982) 587-595.
[47] O.M. Jensen, The pozzolanic reaction of silica fume, MRS Online Proceedings Library Archive 1488 (2012).
[48] T. Gao, B.P. Jelle, A. Gustavsen, S. Jacobsen, Aerogel-incorporated concrete: An experimental study, Construction and Building Materials 52(Supplement C) (2014) 130-136.
[49] C. Page, Ø. Vennesland, Pore solution composition and chloride binding capacity of silica-fume cement pastes, Matériaux et Construction 16(1) (1983) 19-25.
[50] F. Winnefeld, B. Lothenbach, Hydration of calcium sulfoaluminate cements—experimental findings and thermodynamic modelling, Cem. Concr. Res. 40(8) (2010) 1239-1247.
[51] F. Glasser, L. Zhang, High-performance cement matrices based on calcium sulfoaluminate–belite compositions, Cem. Concr. Res. 31(12) (2001) 1881-1886.
[52] D. Sanz-Pont, D. Sanz-Arauz, C. Bedoya-Frutos, R.J. Flatt, S. López-Andrés, Anhydrite/aerogel composites for thermal insulation, Mater. Struct. 49(9) (2016) 3647-3661.
[53] M. Schäper, G. Meier, Die Taupunkt-Falle, Ausbau und fassade 1 (2009) 44-47.
[54] T. Stahl, S. Brunner, M. Zimmermann, K. Ghazi Wakili, Thermo-hygric properties of a newly developed aerogel based insulation rendering for both exterior and interior applications, Energy and Buildings 44(0) (2012) 114-117.
[55] D. Dauti, A. Tengattini, S. Dal Pont, N. Toropovs, M. Briffaut, B. Weber, Analysis of moisture migration in concrete at high temperature through in-situ neutron tomography, Cem. Concr. Res. 111 (2018) 41-55.
[56] D. Dauti, S. Dal Pont, B. Weber, M. Briffaut, N. Toropovs, M. Wyrzykowski, G. Sciumé, Modeling concrete exposed to high temperature: Impact of dehydration and retention curves on moisture migration, International Journal for Numerical and Analytical Methods in Geomechanics 42(13) (2018) 1516-1530.
[57] D. Dauti, S. Dal Pont, M. Briffaut, B. Weber, Modeling of 3D moisture distribution in heated concrete: From continuum towards mesoscopic approach, Int. J. Heat Mass Transfer 134 (2019) 1137-1152.
[58] D. Dauti, B. Weber, S. Dal Pont, A. Tengattini, N. Toropovs, M. Briffaut, First results on fast neutron tomography of heated concrete, 5th Int. Work. Concr. Spalling Due to Fire Expo., Boras, Sweden, 2017, pp. 249–258.
[59] J. Banhart, Advanced tomographic methods in materials research and engineering, Oxford University Press2008.
[60] L.A. Feldkamp, L. Davis, J.W. Kress, Practical cone-beam algorithm, Opt. Soc. Am. 1(6) (1984) 612-619.
[61] G. Reichenauer, Structural Characterization of Aerogels, in: M.A. Aegerter, N. Leventis, M.M. Koebel (Eds.), Aerogels Handbook, Springer New York2011, pp. 449-498.
[62] N. Toropovs, M. Wyrzykowski, P. Lura, Effect of exposure to elevated temperatures on spalling, mechanical properties and transport properties of high-performance mortars, Cem. Concr. Compos. Manuscript in preparation (2019).
[63] J. Kaufmann, R. Loser, A. Leemann, Analysis of cement-bonded materials by multi-cycle mercury intrusion and nitrogen sorption, J. Colloid Interface Sci. 336(2) (2009) 730-737.
[64] I. Odler, M. Rößler, Investigations on the relationship between porosity, structure and strength of hydrated Portland cement pastes. II. Effect of pore structure and of degree of hydration, Cem. Concr. Res. 15(3) (1985) 401-410.
[65] G. Schober, The most important aspects of microstructure influencing strength of AAC, AAC, Taylor & Francis (2005) 145-153.
[66] Y.F. Houst, F.H. Wittmann, Influence of porosity and water content on the diffusivity of CO2 and O2 through hydrated cement paste, Cem. Concr. Res. 24(6) (1994) 1165-1176.
[67] I. Odler, The BET-specific surface area of hydrated Portland cement and related materials, Cem. Concr. Res. 33(12) (2003) 2049-2056.
[68] J.J. Thomas, J.J. Chen, A.J. Allen, H.M. Jennings, Effects of decalcification on the microstructure and surface area of cement and tricalcium silicate pastes, Cem. Concr. Res. 34(12) (2004) 2297-2307.
[69] M.Y. Balshin, Relation of mechanical properties of powder metals and their porosity and the ultimate properties of porous metal-ceramic materials, Dokl Akad Nauk SSSR, 1949, pp. 831-834.
[70] L.F. Nielsen, Strength development in hardened cement paste: examination of some empirical equations, Mater. Struct. 26(5) (1993) 255-260.
[71] E. Kearsley, P. Wainwright, The effect of porosity on the strength of foamed concrete, Cem. Concr. Res. 32(2) (2002) 233-239.

[72] N. Narayanan, K. Ramamurthy, Structure and properties of aerated concrete: a review, Cem. Concr. Compos. 22(5) (2000) 321-329.

[73] E.K. Nambiar, K. Ramamurthy, Models for strength prediction of foam concrete, Mater. Struct. 41(2) (2008) 247.

[74] Comité euro-international du béton, Autoclaved aerated concrete: CEB manual of design and technology, Construction Press1978.

[75] M. Jones, A. McCarthy, Preliminary views on the potential of foamed concrete as a structural material, Magazine of concrete research 57(1) (2005) 21-31.

[76] C. Bing, W. Zhen, L. Ning, Experimental research on properties of high-strength foamed concrete, J. Mater. Civ. Eng. 24(1) (2011) 113-118.

[77] H. Lu, H. Luo, N. Leventis, Mechanical Characterization of Aerogels, in: M.A. Aegerter, N. Leventis, M.M. Koebel (Eds.), Aerogels Handbook, Springer New York, New York, NY, 2011, pp. 499-535.

[78] K.-H. Kim, S.-E. Jeon, J.-K. Kim, S. Yang, An experimental study on thermal conductivity of concrete, Cem. Concr. Res. 33(3) (2003) 363-371.

[79] K. Pietrak, T.S. Wisniewski, A review of models for effective thermal conductivity of composite materials, Journal of Power Technologies 95(1) (2015) 14.

[80] H.J. Böhm, S. Nogales, Mori–Tanaka models for the thermal conductivity of composites with interfacial resistance and particle size distributions, Compos. Sci. Technol. 68(5) (2008) 1181-1187.

[81] D.P. Bentz, A review of early-age properties of cement-based materials, Cem. Concr. Res. 38(2) (2008) 196-204.

[82] S.B. Tatro, Thermal properties, in: J.F. Lamond, J.H. Pielert (Eds.), Significance of tests and properties of concrete and concrete-making materials, STP169D-EB, ASTM West Conshohocken, PA2006.

[83] N. Toropovs, F.L. Monte, M. Wyrzykowski, B. Weber, G. Sahmenko, P. Vontobel, R. Felicetti, P. Lura, Real-time measurements of temperature, pressure and moisture profiles in High-Performance Concrete exposed to high temperatures during neutron radiography imaging, Cem. Concr. Res. 68 (2015) 166-173.

[84] T. Shimizu, K. Kanamori, A. Maeno, H. Kaji, C.M. Doherty, K. Nakanishi, Transparent Ethenylene-Bridged Polymethylsiloxane Aerogels: Mechanical Flexibility and Strength and Availability for Addition Reaction, Langmuir 33(18) (2017) 4543-4550.